https://doi.org/10.5194/essd-2026-860
Preprint. Discussion started: 4 November 2026
© Author(s) 2026. CC BY 4.0 License.



Open Access Earth System Science Data Discussions

SDUST2026SM: a global seamount catalog based on vertical gradient of gravity anomaly and bathymetric data

Yi Gao [1], Jinyun Guo [1*], Shaoshuai Ya [1], Daocheng Yu [2], Xin Liu [1], Cheinway Hwang [3]

1 College of Geodesy and Geomatics, Shandong University of Science and Technology, Qingdao 266590, China
2 School of Geomatics, Liaoning Technical University, Fuxin, 123000, China
3 Department of Civil Engineering, National Yang Ming Chiao Tung University, 1001 Ta Hsueh Road, Hsinchu, 300, Taiwan
* Corresponding to: jinyunguo1@126.com (J. G.)

Abstract. This study applies the integrated seamount detection and height estimation method based on vertical gradient of gravity anomaly (VGGA) and bathymetry (ISDHEB) to detect and catalog seamounts across the global ocean between 80° N and 80° S. This analysis uses the SWOT_04 VGGA field released by the Scripps Institution of Oceanography (SIO) and the GEBCO_2025 bathymetry grid. The global ocean was divided into 10° × 10° processing tiles, each surrounded by a 1° overlapping buffer. Candidate features were screened using multiple constraints, including local maxima, closed contours, area and amplitude, circular or elliptical fitting, Jaccard similarity, and seamount exclusion zones. Marker-controlled watershed segmentation was used to separate multi-peak anomalies. Foot-of-slope points were then identified from the slope and second derivative of bathymetric profiles to estimate base depth and seamount height, followed by visual quality control. A total of 68,934 candidate seamounts at least 100 m high were identified. Small, medium, and large seamounts accounted for 67.6 %, 30.9 %, and 1.5 % of the candidates, respectively. After visual inspection, 67,374 targets were retained in the high-confidence seamount set, corresponding to an overall candidate acceptance rate of 97.74 %. The high-confidence catalog contains 55.0 % more seamounts than the SIO 2023 catalog, with most additional targets having heights below 1 km. The cumulative height-frequency relationship follows a clear power law above 0.8 km but progressively deviates at lower heights. The expanded catalog reflects the combined benefits of SWOT-enhanced gravity information, updated bathymetry, and the integrated detection and height-estimation procedure. The resulting catalog provides a basis for studies of seafloor tectonics, shipborne bathymetric survey

https://doi.org/10.5194/essd-2026-860
Preprint. Discussion started: 4 November 2026
© Author(s) 2026. CC BY 4.0 License.



planning, and marine ecological and resource investigations. The SDUST2026SM dataset is publicly available at https://doi.org/10.5281/zenodo.23277209 (Gao et al., 2026).

1 Introduction

Seamounts are isolated geological features on the seafloor. They were originally defined as isolated submarine volcanoes rising more than 1000 m above the surrounding seafloor (Menard, 1964). More recent definitions include isolated topographic features with relief greater than 100 m, excluding features associated with continental shelves or land. Seamount height is defined as the vertical relief between the summit and the deepest closed contour surrounding the main edifice (International Hydrographic Organization, 2008; Staudigel et al., 2010). Seamounts are important to a broad range of Earth-science studies, including studies of marine ecology, geological processes, and climate change (Clark et al., 2010; Wang et al., 2024; Wei et al., 2024; Ross et al., 2020). Accurate global detection of seamounts and characterization of their morphology are therefore important for a wide range of scientific applications.

Traditional seamount detection relies primarily on multibeam echo sounding, which provides high-accuracy maps of seafloor topography. However, global coverage remains limited because shipborne surveys are costly. Niyazi et al. (2025), based on publicly available information from the Seabed 2030 project, reported that as of June 2024 approximately 26.1 % of the global seafloor met modern mapping standards. Satellite-altimetry-derived marine gravity data provide an alternative means of detecting seamounts. Seamounts perturb the marine gravity field and produce corresponding sea-surface-height anomalies, allowing seafloor features to be inferred indirectly from satellite altimetry (Yu and Hwang, 2022; Sandwell and Smith, 1997; Li et al., 2024). Although these data have lower spatial resolution than direct bathymetric measurements, they provide global coverage. Early global seamount detection and census studies therefore relied largely on altimetry from missions such as Seasat and Geosat (Craig and Sandwell, 1988; Baudry and Calmant, 1991; Kitchingman and Lai, 2004). Estimates of the global seamount population varied considerably because of differences in data resolution and detection methods. In particular, one-dimensional along-track sampling and relatively low signal-to-noise ratios limited the detection of small and medium-sized seamounts (Wessel et al., 2010).

https://doi.org/10.5194/essd-2026-860
Preprint. Discussion started: 4 November 2026
© Author(s) 2026. CC BY 4.0 License.



To detect finer-scale seafloor features, researchers have increasingly used the vertical gradient of gravity anomaly (VGGA) (Sandwell et al., 2014; Sandwell et al., 2022; Wessel and Lyons, 1997). VGGA is the vertical derivative of the gravity anomaly and enhances short-wavelength components of the gravity field, making it particularly sensitive to small-scale seafloor features (Kim and Wessel, 2011). With continued advances in satellite altimetry and data-processing methods, VGGA has become increasingly important for seamount detection (Zhou et al., 2024, 2025). Wessel (2001) used VGGA derived from Geosat and ERS-1 altimetry to characterize seamount distribution across the Pacific Plate and identified 14,675 seamounts. Kim and Wessel (2011) subsequently reprocessed Geosat and ERS-1 altimeter data and combined them with nonlinear inversion techniques to automatically identify and parameterize 24,643 seamounts worldwide. The retrieved parameters included location, peak VGGA amplitude, and the major axis, minor axis, and azimuth of the fitted base. More recently, Gevorgian et al. (2023) generated an updated VGGA using data from CryoSat-2, Envisat, Jason-1, and SARAL/AltiKa. Through visual interpretation and refined analysis, they identified an additional 19,325 seamounts and expanded the global catalog to 43,454 features, while also investigating the morphology of small seamounts. Despite these advances, VGGA derived from conventional nadir altimetry remains constrained by satellite track spacing and measurement noise. Its spatial resolution and signal-to-noise ratio therefore continue to limit the detection of even smaller seamounts.

The Surface Water and Ocean Topography (SWOT) satellite was launched on 16 December 2022 and provides new opportunities to improve VGGA observations. Its primary instrument, the Ka-band Radar Interferometer (KaRIn), simultaneously observes two swaths, each approximately 50 km wide. This configuration substantially increases the two-dimensional sampling density of sea-surface height (Morrow et al., 2019; Ya et al., 2026; Fu et al., 2024; Guo et al., 2024). Using simulated SWOT data, D. Yu et al. (2021) investigated the recovery of the marine gravity field from SWOT altimetry; subsequently, D. Yu et al. (2024) developed an automatic identification and fitting algorithm for seamounts (AIFS). The latter study demonstrated the potential of SWOT data for detecting small seamounts. However, these studies did not use actual SWOT observations and did not systematically estimate seamount morphological parameters.

The present study applies the integrated seamount detection and height estimation method based on VGGA and bathymetry (ISDHEB) (Gao et al., 2026) to the global

https://doi.org/10.5194/essd-2026-860
Preprint. Discussion started: 4 November 2026
© Author(s) 2026. CC BY 4.0 License.



ocean between 80° N and 80° S using SWOT_04 VGGA and GEBCO_2025 data. We perform automatic seamount detection, height estimation, and visual quality control, and further evaluate the size composition, spatial distribution, and detection limitations of the resulting seamount catalog.

The remainder of this paper is organized as follows. Section 2 introduces the SWOT_04 VGGA, GEBCO_2025 bathymetry, and the reference seamount catalog. Section 3 describes the methods used for global seamount detection, height estimation, and visual inspection. Section 4 presents the global detection results, seamount height-frequency distribution, spatial variation, visual inspection results, and comparison with the reference catalog. Section 5 discusses the expansion of the catalog, limitations in small-seamount detection, bathymetric coverage, tectonic implications, and uncertainties. Section 6 summarizes the main conclusions.

2 Study Data

2.1 VGGA data

This study uses the global marine gravity field product released by the Scripps Institution of Oceanography (SIO), University of California, San Diego. Specifically, we use the SWOT_04 VGGA grid with a grid spacing of 1′ × 1′.

Compared with earlier versions, SWOT_04 VGGA incorporates improvements in both multi-source data integration and noise-reduction algorithms. In terms of data coverage, SWOT_04 incorporates observations from the 1-day repeat orbit and the first 18 cycles of the 21-day science orbit. Compared with version 03, SWOT_04 incorporates an additional 12 months of SWOT science-phase observations, bringing the cumulative extension to 17 months. The V33 altimetry-derived gravity product was used as the background gravity field. V33 incorporates 30 months of multi-mission altimetry data from AltiKa, CryoSat-2 in LRM and SAR modes, Jason-2, Sentinel-3A/B, and other missions (Sandwell et al., 2021). The SWOT_04 product is available at https://topex.ucsd.edu/pub/global_grav_1min_SWOT/curv_SWOT_04.nc.

2.2 Bathymetric data

We use GEBCO_2025, a global topographic model released by the General Bathymetric Chart of the Oceans (GEBCO) (GEBCO Compilation Group, 2025). It is a global elevation grid with a spacing of 15 arcsec. GEBCO_2025 uses SRTM15+V2.7 as its base grid (Tozer et al., 2019), which combines land topography with measured and predicted bathymetry. GEBCO_2025 further incorporates additional bathymetric

https://doi.org/10.5194/essd-2026-860
Preprint. Discussion started: 4 November 2026
© Author(s) 2026. CC BY 4.0 License.



datasets, primarily high-resolution multibeam bathymetry. The product also provides a Type Identifier (TID) grid that records the source of the topographic information. In this study, ocean grid cells with TID values of 10–17 are classified as directly measured, whereas the remaining cells are classified as indirectly derived because their bathymetry is based on satellite-gravity prediction or spatial interpolation(GEBCO Compilation Group, 2025). GEBCO_2025 and its TID information are available at https://www.gebco.net/data-products/gridded-bathymetry-data.

2.3 Reference seamount catalog

We use the global seamount catalog released by SIO in 2023 as the reference catalog (Gevorgian et al., 2023). The catalog was compiled using visual interpretation of the V30 VGGA grid and contains 43,454 seamounts. The catalog is available at https://zenodo.org/records/7718512.

3 Global seamount detection and height estimation methods

We apply the integrated seamount detection and height estimation method based on VGGA and bathymetry (ISDHEB; Gao et al., 2026) to identify seamounts globally. The procedure consists of four main steps: dividing the global ocean into tiles and identifying potential seamount centers from the VGGA grid; screening closed VGGA contours using multiple criteria and separating multi-peak anomalies; estimating seamount heights from bathymetric profiles; and visual inspection.

3.1 Global tile-based processing

The ocean between 80° N and 80° S is divided into 576 processing tiles of 10° × 10°. Each tile is expanded by a 1° buffer on all sides during processing. After processing, only detections within the central 10° × 10° area of each tile are retained, and duplicate detections are removed when the global results are merged.

A two-dimensional Gaussian filter is applied to the VGGA field within each processing tile:

$$G(x,y)=\frac{1}{2\pi\sigma^2}\cdot \mathrm{e}^{-\frac{x^2+y^2}{2\sigma^2}} \tag{1}$$

where x and y denote the grid coordinates and σ is the standard deviation of the Gaussian kernel. In this study, σ was set to 1.4 grid cells along both coordinate axes, corresponding to 1.4′ in the 1′ × 1′ VGGA grid. Potential seamount centers are then

https://doi.org/10.5194/essd-2026-860
Preprint. Discussion started: 4 November 2026
© Author(s) 2026. CC BY 4.0 License.



identified as local maxima in the smoothed VGGA field. VGGA contours are generated at an interval of 1 E (1 E = 10^{-9} s^{-2}).

3.2 Candidate contour screening and multi-peak anomaly segmentation

Closed VGGA contours are screened sequentially using the following criteria. (1) Contours containing a single potential seamount center are screened directly, whereas those containing two to five VGGA peaks are subjected to watershed segmentation. (2) The contour area must be at least 50 km² (Kim and Wessel, 2011). (3) The VGGA amplitude must be at least 12 E, defined as

$$A = VGGA_{r_i} - VGGA_{m_i} \tag{2}$$

where $VGGA_{ri}$ is the VGGA value at potential center r_i and $VGGA_{mi}$ is the VGGA value of contour m_i. The amplitude threshold of 12 E is approximately three times the standard deviation of background fluctuations (3.6-3.7 E) in areas without distinct seamount topography.

(4) Each contour is fitted with a circle or an ellipse. The area error is defined as

$$S_{error} = \frac{\left| S_{m_i} - S_{circle/ellipse} \right|}{S_{circle/ellipse}} \times 100\% \tag{3}$$

where S_{m_i} is the area enclosed by the VGGA contour and $S_{circle/ellipse}$ is the area of the fitted circle or ellipse. The area errors of both the circular and elliptical fits must be less than 10 %.The Jaccard similarity coefficient is also used to quantify the overlap between the contour and the fitted shape:

$$J(m_i, B) = \frac{\left| S_{m_i} \cap S_{circle/ellipse} \right|}{\left| S_{m_i} \cup S_{circle/ellipse} \right|} \tag{4}$$

where J is the Jaccard similarity coefficient. Contours with J < 0.6 are discarded. (5) Following the 2000 m depth criterion of Kim and Wessel (2011), seamount exclusion zones (SEZs) are defined using GEBCO_2025 bathymetry. Candidate seamounts located within these zones or their 20 km buffers are excluded.

For contours containing two to five potential seamount centers, these centers are used as markers for marker-controlled watershed segmentation of the negative VGGA field (−VGGA) (Gonzalez and Woods, 2017). The screening procedure described above is then repeated for each segmented subregion. For each potential seamount center that

https://doi.org/10.5194/essd-2026-860
Preprint. Discussion started: 4 November 2026
© Author(s) 2026. CC BY 4.0 License.



passes all screening criteria, the outermost closed VGGA contour satisfying these criteria is selected as the seamount base contour.

3.3 Seamount height estimation from bathymetric data

Seamount height H is calculated from the summit depth D_{top} and base depth D_{base} as follows:

$$H = \left| D_{top} - D_{base} \right| \tag{5}$$

Within each seamount base contour, the location of the shallowest grid cell in GEBCO_2025 is taken as the seamount summit. Bathymetric profiles are extracted in the meridional and zonal directions, and the slope and second derivative of each profile are calculated. Extrema of the second derivative are selected as candidate foot-of-slope points (Wu et al., 2014). Candidate foot-of-slope points are then screened using depth, slope, and position criteria. The depth thresholds are determined using a two-threshold Otsu method (Otsu, 1979), with the between-class variance defined as follows:

$$\sigma_b^2(k_1, k_2) = \sum_{i=1}^{3} \omega_i (\mu_i - \mu_{total})^2 \tag{6}$$

Here, k_1 and k_2 ($k_1 < k_2$) are the depth thresholds, and σ_b^2 (k_1, k_2) is the between-class variance. μtotal is the overall mean depth. For class i, μ_i is the mean depth and ω_i is the sample proportion. We test possible combinations of k_1 and k_2 and select the pair that maximizes the between-class variance σ_b^2. Only candidate foot-of-slope points with slopes below 7° and located in the transition from the seamount flanks to the base are retained (Gao et al., 2026). The base depth D_{base} is estimated as the median depth of all valid foot-of-slope points. Seamount height H is then calculated using Eq. (5).

3.4 Visual inspection

All automatically detected candidates are subjected to visual inspection. Visual inspection examines whether VGGA anomalies correspond to bathymetric relief in GEBCO_2025, whether the bathymetric contours are closed, whether each candidate is topographically isolated, and whether foot-of-slope points can be identified. Candidates are rejected if they form part of linear ridges or other continuous geological structures associated with mid-ocean ridges or fracture zones. They are also rejected when

https://doi.org/10.5194/essd-2026-860
Preprint. Discussion started: 4 November 2026
© Author(s) 2026. CC BY 4.0 License.



bathymetric relief is insufficient or no valid foot-of-slope points can be identified. Candidates near the boundaries of the SEZ buffers are examined separately to determine whether they form part of continental shelves or adjacent landmasses.

4 Results and analysis

4.1 Global automatic detection results and catalog composition

Applying ISDHEB to the global ocean between 80° N and 80° S yields 68,934 automatically detected candidate seamounts with heights of at least 100 m. To distinguish between the initial detections and the results after visual inspection, we refer to the former as the automatically detected candidate set and the latter as the high-confidence seamount set. The candidate set is mainly used to assess the detection results for seamounts of different sizes and to analyze their morphological characteristics, whereas the high-confidence seamount set is recommended for further applications.

The detected seamounts are classified into three height groups: small ($0.1\ \text{km} \le H < 1\ \text{km}$), intermediate ($1\ \text{km} \le H < 3\ \text{km}$), and large ($H \ge 3\ \text{km}$) seamounts. Among the 68,934 detected candidates, 46,620 are small seamounts (67.6 %), 21,291 are intermediate seamounts (30.9 %), and 1,023 are large seamounts (1.5 %). Small seamounts outnumber intermediate and large seamounts combined by a factor of approximately 2.1, indicating that the expansion of the catalog is mainly associated with seamounts less than 1 km high.

The numbers in each class are listed in Table 1.

Table 1. Global height-class composition of the automatically detected seamount candidate set

Height class	Height range (km)	Number	Proportion (%)
Small seamounts	$0.1 \le H < 1$	46,620	67.6
Medium seamounts	$1 \le H < 3$	21,291	30.9
Large seamounts	$H \ge 3$	1,023	1.5
Total	$H \ge 0.1$	68,934	100.0

Candidate seamounts form pronounced belts, chains, and clusters across the global ocean (Fig. 1). Small seamounts are widespread on the flanks of mid-ocean ridges, near transform faults, and within abyssal basins. Medium and large seamounts are more concentrated in intraplate volcanic chains, oceanic plateaus, and island-arc systems in the central and western Pacific. This size-dependent pattern is broadly consistent with the spatial distributions reported in previous global VGGA-based seamount studies (Kim and Wessel, 2011; Gevorgian et al., 2023).

https://doi.org/10.5194/essd-2026-860
Preprint. Discussion started: 4 November 2026
© Author(s) 2026. CC BY 4.0 License.



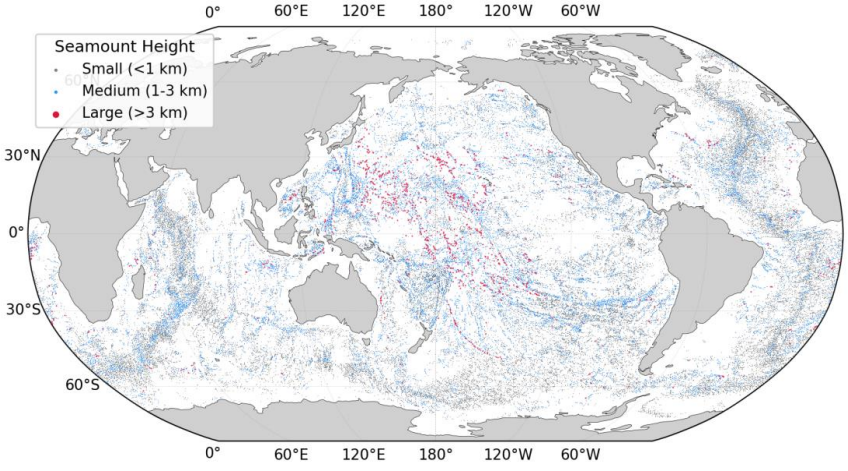


Figure 1. Global distribution and height classes of automatically detected seamount candidates

The SDUST2026SM catalog was compiled using a 1′ × 1′ analysis grid. Each catalog entry includes the seamount center location, height, base depth, semi-major and semi-minor axes, azimuth of the major axis, peak VGGA amplitude, and a unique seamount identifier. The catalog therefore provides both feature locations and a consistent set of parameters for subsequent morphological statistics, tectonic regional analysis, and shipborne survey planning.

4.2 Seamount height-frequency distribution

Candidate seamount heights range from 100 to 6,308 m, with a mean of 929.7 m and a median of 781 m. The mean exceeds the median, indicating a clearly right-skewed distribution. The 25th and 75th percentiles are 533 and 1,133.5 m, respectively, so half of the candidates lie between approximately 0.53 and 1.13 km. With a bin width of 200 m, the 500–700 m height interval contains the largest number of candidate seamounts (13,998). The number decreases rapidly with increasing height above this interval.

Figure 2a shows that small seamounts dominate the height-frequency distribution, whereas seamounts at least 3 km high account for only a small fraction. The lower height limit for power-law fitting was determined from the transition between the curved and approximately linear portions of the cumulative height-frequency distribution on a log–log plot. For $H \geq 0.8$ km, the data follow an approximately linear trend on the log–log plot. We therefore selected 0.8 km as the empirical lower height limit for the power-law fit. Above this value, the cumulative number is well described by a power-law relationship:

https://doi.org/10.5194/essd-2026-860
Preprint. Discussion started: 4 November 2026
© Author(s) 2026. CC BY 4.0 License.



Open Access Earth System Science Data Discussions

$$N(\geq H) = C \cdot H^{-\beta} \tag{7}$$

Here, N(≥H) is the cumulative number of seamounts with height greater than or equal to H. C is a proportionality constant, and β is the decay exponent of the cumulative frequency. In log N versus log H space, the fitted line has a slope of -β; a larger β indicates a faster decrease in cumulative number with increasing height. We obtain β = 2.65 and a coefficient of determination $R^2 = 0.952$ (Fig. 2b). Below 0.8 km, the observed cumulative counts progressively deviate from the fitted power law, and the curve becomes flatter. The number of detected seamount candidates in this height range is lower than that predicted by extrapolating the power-law relationship.

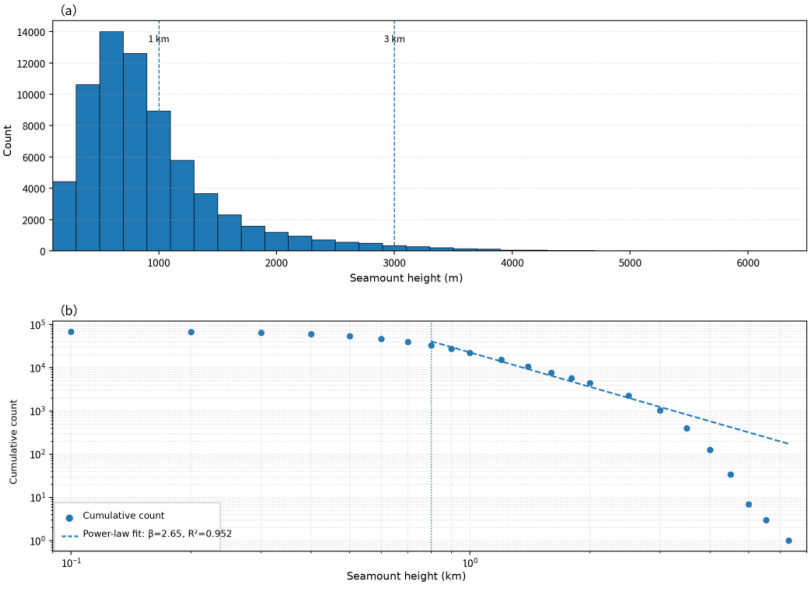


Figure 2. Global seamount height-frequency characteristics: (a) seamount height-frequency distribution; (b) log-log distribution of seamount height and cumulative frequency with the power-law fit

4.3 Global spatial variation and plate-scale statistics

The number of detected seamounts on each tectonic plate is strongly influenced by the area of purely oceanic crust. Using the PB2002 global plate model (Bird, 2003), we assigned the detected seamounts to individual tectonic plates. The Pacific Plate contains 19,483 detected seamounts, accounting for 28.3 % of the candidate set and representing the largest number among all plates. The Antarctic, African, and Australian plates contain 9,612, 8,239, and 6,889 seamounts, respectively. These plates all contain

https://doi.org/10.5194/essd-2026-860
Preprint. Discussion started: 4 November 2026
© Author(s) 2026. CC BY 4.0 License.



large areas of purely oceanic crust; consequently, high absolute counts do not necessarily indicate a higher seamount abundance per unit area.

After normalization by the area classified as purely oceanic crust, the plate ranking changes markedly (Fig. 3). The Philippine Sea Plate has the highest seamount density, close to 300 seamounts per 10^6 km². The Nazca and Pacific plates follow at approximately 248 and 232 seamounts per 10^6 km², respectively. Although the Philippine Sea Plate contains only 1,623 detected seamounts, its relatively small area of purely oceanic crust results in a higher seamount density than that of the Pacific Plate. The Philippine Sea Plate is also characterized by complex trench–arc–basin systems and back-arc spreading centers. In contrast, the Eurasian, Arabian, and Amur plates are dominated by continental crust. Their areas of purely oceanic crust and detectable ocean regions are smaller, so their normalized densities are generally lower.

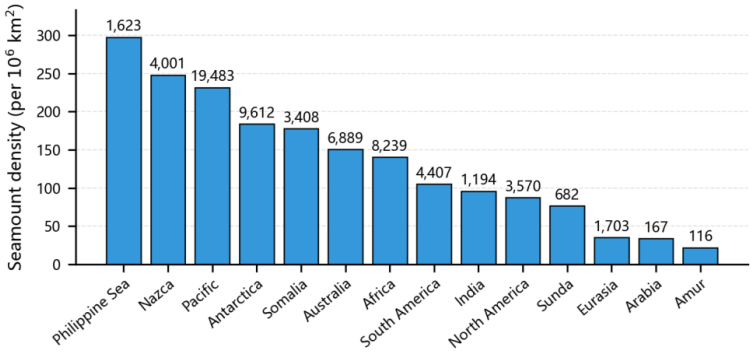


Figure 3. Ranking of seamount density over areas of purely oceanic crust for major global tectonic plates

Plate-scale density reflects both the tectonic setting of seamount formation and the effects of seamount exclusion zones, water depth, sediment cover, and data quality. Figure 3 therefore represents the observed seamount density in the catalog and should not be interpreted directly as the true volcanic production rate of each plate.

4.4 Visual inspection results

To evaluate the reliability of the automatic detections, we use the GEBCO_2025 TID grid (GEBCO Compilation Group, 2025) to group candidates by bathymetric data source. A candidate is assigned to the directly measured group when directly measured bathymetry covers at least 50 % of the area inside its base contour. All other candidates are assigned to the indirectly derived group. Of the 68,934 candidates, 20,846 (30.2 %)

https://doi.org/10.5194/essd-2026-860
Preprint. Discussion started: 4 November 2026
© Author(s) 2026. CC BY 4.0 License.



belong to the directly measured group and 48,088 (69.8 %) to the indirectly derived group.

Visual inspection assesses the correspondence between seamount contours and bathymetric relief, as well as the spatial independence of each candidate. We also check for closed bathymetric contours, connections to linear tectonic structures, and identifiable foot-of-slope points. After visual inspection, 67,374 seamounts were retained in the high-confidence seamount catalog, accounting for 97.74 % of the automatically detected candidates. The remaining 1,560 candidates (2.26 %) were rejected. In the directly measured group, 20,436 targets are accepted, corresponding to an acceptance rate of 98.03 %. In the indirectly derived group, 46,938 targets are accepted, corresponding to 97.61 %. The difference between the two acceptance rates is only 0.42 percentage points, showing that the two groups have similar acceptance rates under the current screening and visual-inspection criteria. The statistics are listed in Table 2.

Table 2. Visual inspection results for global seamount candidates

Coverage type	Candidates	Accepted	Rejected	Rate (%)
Directly measured	20,846	20,436	410	98.03
Indirectly derived	48,088	46,938	1,150	97.61
Total	68,934	67,374	1,560	97.74

Bathymetry for the directly measured group is derived primarily from multibeam, single-beam, and other direct measurements, which provide more direct information on topographic morphology and foot-of-slope locations. The 98.03 % acceptance rate indicates that most candidates in the directly measured group were retained after visual inspection. The remaining visual checks focus mainly on complex tectonic boundaries and topographic independence. This acceptance rate is an internal quality-control metric for an already screened candidate set and should not be interpreted as a detection rate or precision estimate based on a complete global ground-truth sample. The 410 rejected targets in the directly measured group are not uniformly distributed in space; they are concentrated near plate boundaries and mid-ocean ridges, at transitions between trenches and abyssal plains, and in high-latitude regions (Fig. 4). Strong topographic gradients and closely spaced tectonic units in these settings can generate closed VGGA anomalies similar to those produced by isolated seamounts.

The overall acceptance rate of 97.74% represents the consistency of automatically detected candidates with the adopted screening and visual-inspection criteria, rather

https://doi.org/10.5194/essd-2026-860
Preprint. Discussion started: 4 November 2026
© Author(s) 2026. CC BY 4.0 License.



than independently validated detection precision. Because visual inspection also relies on GEBCO_2025 bathymetry, this assessment is not independent of the data used in candidate screening and height estimation. This limitation is particularly relevant to the 69.8% of candidates located in areas with predominantly indirectly derived bathymetry.

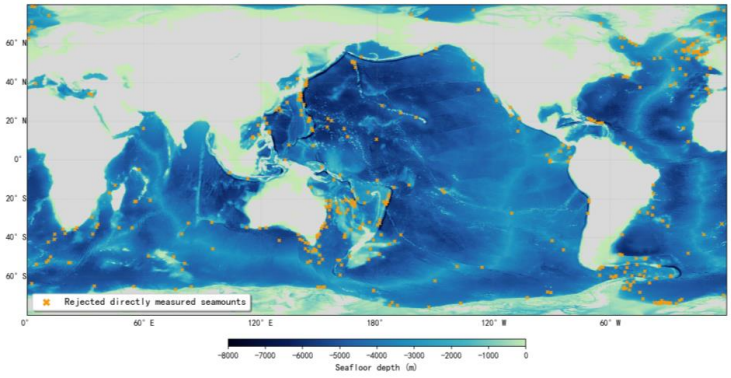


Figure 4. Global distribution of targets in the directly measured group that failed visual inspection

4.5 Comparison with the reference seamount catalog

To evaluate the spatial correspondence between SDUST2026SM and the SIO 2023 catalog, we adopted a center-in-contour matching criterion. Each seamount center in the SIO 2023 catalog was considered spatially matched if it fell within at least one SDUST2026SM base contour. Each SIO 2023 entry was counted only once, regardless of the number of SDUST2026SM contours containing its center. No strict one-to-one correspondence was imposed, as multiple SIO 2023 seamount centers could fall within the same SDUST2026SM base contour. Under this criterion, 41,950 of the 43,454 SIO 2023 entries were spatially matched, corresponding to a spatial inclusion rate of 96.54%. The remaining 1,504 entries did not satisfy this criterion.

Based on their bathymetric expression in GEBCO_2025, the 1,560 candidates rejected by visual inspection can be divided into two categories. The first category shows local VGGA anomalies but lacks independent bathymetric relief of at least 100 m in the current GEBCO_2025 model. The second category shows clear bathymetric variation but forms part of a continuous geological structure, such as a mid-ocean ridge, fracture zone, trench slope, or terrace. These targets therefore do not satisfy the spatial-independence criterion for a seamount.

Within the directly measured group, 158 rejected targets (38.5 %) show no clear bathymetric relief, whereas 252 (61.5 %) correspond to other geological structures. In

https://doi.org/10.5194/essd-2026-860
Preprint. Discussion started: 4 November 2026
© Author(s) 2026. CC BY 4.0 License.



the indirectly derived group, the two categories contain 565 and 585 targets, accounting for 49.1 % and 50.9 %, respectively. Combining both groups, 723 rejected targets (46.3 %) show no clear bathymetric relief and 837 (53.7 %) correspond to other geological structures (Table 3).

Table 3. Types of targets that failed visual inspection

Coverage type	No clear bathymetric relief	Other geological structures	Total
Directly measured	158 (38.5 %)	252 (61.5 %)	410
Indirectly derived	565 (49.1 %)	585 (50.9 %)	1,150
Total	723 (46.3 %)	837 (53.7 %)	1,560

Among all rejected targets, 202 are also listed in the SIO 2023 reference catalog, including 15 in the directly measured group and 187 in the indirectly derived group. Comparison with the current GEBCO_2025 bathymetry indicates three main reasons for these discrepancies: insufficient bathymetric relief, offsets in catalog center locations, and differences in target merging or splitting. Of these targets, 92.6 % belong to the indirectly derived group, indicating lower inter-catalog consistency in areas without direct bathymetric constraints.

5 Discussion

5.1 Expansion relative to existing global seamount catalogs

Kim and Wessel (2011) identified 24,643 potential seamounts at least 100 m high using an earlier VGGA product. Gevorgian et al. (2023) combined V30 VGGA with visual interpretation and expanded the global catalog to 43,454 seamounts. The automatic-detection candidate set in this study contains 68,934 targets, and the high-confidence set after visual inspection contains 67,374 targets. Relative to the SIO 2023 catalog, the candidate and high-confidence sets are larger by 58.6 % and 55.0 %, respectively; relative to the Kim-Wessel catalog, they are larger by 179.7 % and 173.4 %. These percentages should be interpreted cautiously because the catalogs differ in data versions, detection thresholds, seamount exclusion zones, and manual interpretation rules. The reported increases therefore reflect the combined effects of the data and compilation workflow and should not be treated as a direct comparison of the performance of a single algorithm.

The larger catalog primarily reflects two factors. First, SWOT wide-swath altimetry adds short-wavelength information on sea-surface height, while the background gravity field has also improved (Sandwell et al., 2021; Y. Yu et al., 2024).

https://doi.org/10.5194/essd-2026-860
Preprint. Discussion started: 4 November 2026
© Author(s) 2026. CC BY 4.0 License.



Compared with conventional along-track altimetry, KaRIn wide-swath observations substantially increase spatial sampling density, enabling some small-scale VGGA anomalies that were previously close to the noise level to be identified. Second, ISDHEB does not rely solely on gravity-anomaly peaks. It jointly uses closed VGGA contours, area, amplitude, shape similarity, spatial exclusion zones, and GEBCO bathymetric foot-of-slope constraints. Watershed segmentation of multi-peak anomalies further improves the separation of neighboring targets within dense seamount groups.

5.2 Completeness of small-seamount detection and seafloor-age effects

The cumulative height-frequency curve follows a clear power-law pattern above 0.8 km and progressively flattens at lower heights. Together with the upward-continuation effect inherent in satellite gravity and the noise characteristics of VGGA, this pattern indicates decreasing detection completeness for smaller targets. Seamount gravity signals weaken at shorter wavelengths and greater water depths. At the same time, VGGA amplifies short-wavelength signals from altimetry noise, abyssal hills, and fracture structures (Kim and Wessel, 2011). Small and deep seamounts are therefore more difficult to distinguish from background signals and non-volcanic topography. The 0.8 km level is best interpreted as an empirical transition below which incompleteness increasingly affects the statistical distribution of the catalog, rather than as a strict detection limit.

The statistical relationship between seamount density and seafloor age further supports this interpretation (Fig. 5). The highest observed density occurs on young oceanic crust aged 0-10 Ma and generally decreases with increasing crustal age. This trend may partly reflect near-ridge volcanism: young, thin, and highly fractured lithosphere favors small-scale magma ascent and the formation of numerous small volcanic edifices (Fornari et al., 1988). Older oceanic crust is also generally deeper and more heavily covered by sediment, conditions that can attenuate or obscure the gravity and bathymetric signals of small seamounts. Across most age intervals, the observed density in our catalog exceeds that of the SIO 2023 catalog, consistent with the identification of more seamount candidates under the updated data products and detection workflow.. However, the systematic incompleteness caused by deep water and sediment cover is not eliminated. The decrease in density with age may therefore combine genuine differences in volcanic production and preservation with substantial

https://doi.org/10.5194/essd-2026-860
Preprint. Discussion started: 4 November 2026
© Author(s) 2026. CC BY 4.0 License.



detection bias and should not be used alone to infer changes in seamount volcanism with oceanic-crust age.

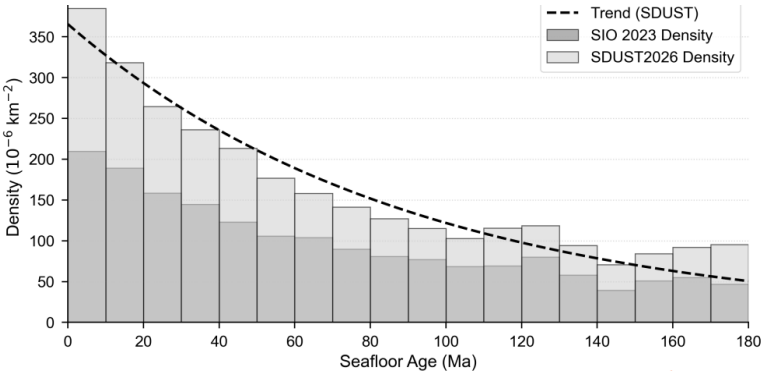


Figure 5. Variation in observed seamount density with seafloor age and comparison with the SIO 2023 catalog

5.3 Shipborne bathymetric coverage and applications of the catalog

Although shipborne multibeam bathymetry provides the most accurate seafloor topography, its global coverage remains sparse. Our statistics show that only 30.2 % of candidate seamounts have more than half of their base area covered by directly measured bathymetry. Nearly 70 % of the targets occur in areas represented mainly by gravity-derived or interpolated bathymetry. Differences in shipborne coverage are particularly pronounced among seamount height classes (Fig. 6): about half of the small seamounts have no shipborne coverage at all, whereas the corresponding fraction for large seamounts is about one-tenth. Medium seamounts fall between these two groups.

In Fig. 6, shipborne bathymetric coverage is defined as the fraction of the seamount base area represented by directly measured bathymetry, $\Delta s = Adirect/Abase \times 100$ %. Here, Adirect is the area within the base contour occupied by grid cells classified as directly measured by the TID, and Abase is the total area within the seamount base contour. For each height class, the normalized count on the vertical axis is expressed as the cumulative proportion $F(\delta) = n(\Delta s \leq \delta)/ntotal \times 100$ %. This quantity represents the percentage of seamounts in that height class with shipborne coverage not exceeding δ.

https://doi.org/10.5194/essd-2026-860
Preprint. Discussion started: 4 November 2026
© Author(s) 2026. CC BY 4.0 License.

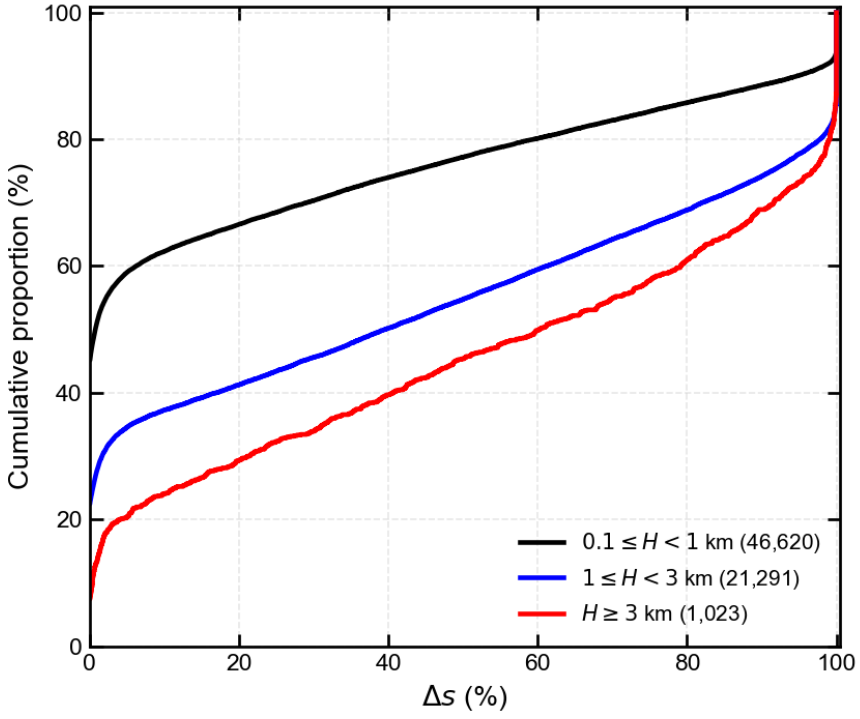


Figure 6. Cumulative distribution of shipborne bathymetric coverage for different seamount height classes

The presence of a ship track does not imply complete mapping. For geometrically small seamounts, a single track or a sparse set of tracks often samples only part of the edifice. Such tracks may not cross the summit or adequately sample the full basal area, and therefore cannot fully constrain seamount height and morphology. Large seamounts have stronger gravity and bathymetric signals and are much more likely to have shipborne coverage. The center locations and size parameters in the new catalog can help identify unmapped or poorly mapped targets and support multibeam survey design, bathymetric model updates, and marine ecological and mineral-resource investigations. In areas with indirectly derived bathymetry, however, these parameters should be treated as prior information for survey planning and prioritization rather than as a substitute for high-resolution shipborne bathymetry.

5.4 Tectonic implications and limits of interpreting global seamount distribution

Plate-scale statistics show that absolute seamount counts and densities normalized by the area classified as purely oceanic crust describe different aspects of seamount distribution. Absolute counts are controlled primarily by the effective area of oceanic

https://doi.org/10.5194/essd-2026-860
Preprint. Discussion started: 4 November 2026
© Author(s) 2026. CC BY 4.0 License.


crust and the detectable area of each plate, whereas area-normalized density is more sensitive to local tectonic settings and the spatial concentration of magmatic activity. The high absolute count on the Pacific Plate should therefore not be interpreted simply as evidence of the strongest volcanic activity per unit area. Likewise, the high densities on the Philippine Sea and Nazca plates may jointly reflect trench-arc-basin systems, back-arc spreading, hotspot-ridge interactions, and complex plate boundaries.

The spatial distribution of the different height classes further indicates that seamount formation is jointly controlled by magma supply and lithospheric state. Small seamounts are more abundant near mid-ocean ridges and on young oceanic crust, where thin and fractured lithosphere may favor dispersed and intermittent magma ascent. Medium and large seamounts are proportionally more common in intraplate hotspot chains, oceanic plateaus, and island-arc systems; this pattern may reflect more concentrated and sustained magma supply and longer growth periods (Kim and Wessel, 2011; Gevorgian et al., 2023; Fornari et al., 1988). This size-dependent pattern is consistent with the seafloor-age relationship discussed above. However, the observed spatial pattern also incorporates preservation and detectability effects related to water depth, sediment cover, and data resolution.

The results therefore support an interpretation in which multiple tectonic environments jointly control the global distribution of seamounts. However, catalog locations and morphological parameters alone cannot uniquely determine the origin of an individual seamount, nor can point density be converted directly into magma production rates. Further discrimination among near-ridge, hotspot-related, and subduction-related origins requires additional information on seamount ages, the geochemistry of seamount rocks, crustal thickness, spreading rates, and seismic structure.

5.5 Uncertainty in height estimation and catalog completeness

Seamount height is estimated from the difference between summit depth and the base depth derived from foot-of-slope points in GEBCO_2025. Its reliability depends mainly on the source and effective resolution of the bathymetric data. The VGGA peak is used only to indicate the center of the gravity anomaly and does not necessarily coincide with the shallowest point of the seamount. Accordingly, the water depth at the VGGA peak is not used directly as summit depth. Instead, the shallowest GEBCO_2025 grid cell within the identified base contour is selected. Bathymetric profiles, slope and

https://doi.org/10.5194/essd-2026-860
Preprint. Discussion started: 4 November 2026
© Author(s) 2026. CC BY 4.0 License.


second-derivative constraints, and the median foot-of-slope depth are used to improve the robustness of height estimation. Targets without identifiable foot-of-slope points are removed during visual inspection. However, globally uniform and independent high-resolution bathymetric ground truth is unavailable, so a single upper bound on height error cannot be provided. Estimates require particular caution where directly measured coverage is limited, where heights are close to the 100 m threshold, or where targets lie in complex tectonic settings. In these cases, height and base dimensions should be regarded as estimates pending verification by shipborne surveys.

Catalog completeness is also scale- and location-dependent. The cumulative distribution deviates from the power law below 0.8 km, seamount density decreases on deep and old oceanic crust, and targets within seamount exclusion zones are deliberately removed. Together, these factors show that the catalog is neither an unbiased nor a complete sample of the global seamount population (Kim and Wessel, 2011; Gevorgian et al., 2023). The high-confidence set is therefore suitable for global distribution statistics, tectonic comparisons, and survey prioritization. Applications involving engineering safety assessments of individual seamounts, detailed volume estimates, or resource assessment should still rely on dedicated multibeam bathymetric and geophysical surveys.

6 Conclusions

Using the SWOT_04 VGGA grid and GEBCO_2025 bathymetry, we applied ISDHEB to the global ocean between 80° N and 80° S and compiled the SDUST2026SM seamount catalog. The automated search identified 68,934 candidates with heights of at least 100 m, of which 67,374 were retained after visual inspection. Small seamounts below 1 km account for 67.6 % of the candidates. Compared with the SIO 2023 catalog, the high-confidence catalog contains 55.0 % more seamounts, with most of the additional detections occurring below 1 km. The increase in catalog size reflects the combined influence of SWOT-enhanced VGGA information, updated bathymetric data, and the integrated detection and height-estimation procedure. Because the reference and present catalogs differ in their input data and processing methodologies, the contribution of SWOT observations alone cannot be quantified from this comparison.

The resulting catalog shows a clear scale dependence in seamount detectability. The cumulative height-frequency distribution is approximately described by a power

https://doi.org/10.5194/essd-2026-860
Preprint. Discussion started: 4 November 2026
© Author(s) 2026. CC BY 4.0 License.



law above 0.8 km, whereas the observed number of seamounts increasingly falls below the extrapolated relationship at smaller heights. Seamount density is highest on young oceanic crust and generally decreases with seafloor age, although this pattern reflects both differences in volcanic setting and variations in detectability caused by water depth, sediment cover, and attenuation of short-wavelength gravity signals. Only 30.2 % of the candidates have at least half of their basal area covered by directly measured bathymetry, but the visual acceptance rates of the directly measured and indirectly derived groups are similar (98.03 % and 97.61 %, respectively).

SDUST2026SM should therefore be regarded as a high-confidence observational catalog rather than a complete census of the global seamount population. Detection of small and deep seamounts remains insufficient, and estimates of height and basal dimensions are less well constrained where bathymetry is derived mainly from gravity prediction or interpolation. Within these limitations, SDUST2026SM provides an updated global representation of seamount locations and dimensions that can be used for large-scale distribution and tectonic analyses and, in particular, for identifying targets that warrant future shipborne bathymetric surveys. Detailed studies of individual seamounts will still require high-resolution multibeam bathymetry and complementary geophysical observations.

Data availability

The SDUST2026SM global seamount catalog is publicly available at https://doi.org/10.5281/zenodo.23277209 (Gao et al., 2026). The dataset contains 68,934 automatically detected seamount candidates with heights of at least 100 m, of which 67,374 were retained after visual inspection.

Author contributions.

YG and JG designed the study. YG implemented the seamount detection and height estimation method, carried out the data analysis, and prepared the manuscript. SY collected and processed the marine gravity and bathymetric datasets. DY contributed to the methodology and validation. XL contributed to the quality assessment of the seamount catalog and the interpretation of the results. CH provided scientific guidance on marine gravity and seamount detection and contributed to the revision of the manuscript. All authors reviewed and approved the manuscript.

https://doi.org/10.5194/essd-2026-860
Preprint. Discussion started: 4 November 2026
© Author(s) 2026. CC BY 4.0 License.



Competing interests.

The authors declare that they have no conflict of interest.

Acknowledgements

We thank the Scripps Institution of Oceanography (SIO) for providing the SWOT_04 vertical gradient of gravity anomaly (VGGA) grid and the SIO 2023 global seamount catalog. We also acknowledge the GEBCO Compilation Group for providing the GEBCO_2025 bathymetric grid and the corresponding Type Identifier (TID) data. We are grateful to NASA and CNES for the SWOT mission, whose wide-swath altimetry observations contributed to the development of the SWOT_04 VGGA product.

References

Baudry, N. and Calmant, S.: 3-D modelling of seamount topography from satellite altimetry, Geophysical Research Letters, 18(6), 1143-1146, 1991.

Bird, P.: An updated digital model of plate boundaries, Geochemistry, Geophysics, Geosystems, 4(3), 1027, https://doi.org/10.1029/2001GC000252, 2003.

Clark, M. R., Rowden, A. A., Schlacher, T., et al.: The ecology of seamounts: Structure, function, and human impacts, Annual Review of Marine Science, 2, 253-278, https://doi.org/10.1146/annurev-marine-120308-081109, 2010.

Craig, C. H. and Sandwell, D. T.: Global distribution of seamounts from Seasat profiles, Journal of Geophysical Research, 93(B9), 10408-10420, 1988.

Fornari, D. J., Perfit, M. R., Allan, J. F., et al.: Small-scale heterogeneities in depleted mantle sources: near-ridge seamount lava geochemistry and implications for mid-ocean-ridge magmatic processes, Nature, 331(6156), 511-513, 1988.

Fu, L.-L., Pavelsky, T., Crétaux, J.-F., et al.: The Surface Water and Ocean Topography Mission: A breakthrough in radar remote sensing of the ocean and land surface water, Geophysical Research Letters, 51(4), e2023GL107652, 2024.

Gao, Y., Guo, J., Ya, S., Yu, D., Liu, X., and Hwang, C.: SDUST2026SM: A Global Seamount Catalog Based on Vertical Gradient of Gravity Anomaly and Bathymetric Data, Zenodo [data set], https://doi.org/10.5281/zenodo.23277209, 2026.

Gao, Y., Liu, X., Yu, D., et al.: An automated seamount detection method integrating vertical gravity gradient anomaly and seafloor topographic models, Acta Geodaetica et Cartographica Sinica, 55(4), 647-657, https://doi.org/10.11947/j.AGCS.2026.20250319, 2026.

GEBCO Compilation Group: GEBCO 2025 Grid [data set], https://doi.org/10.5285/37c52e96-24ea-67ce-e063-7086abc05f29, 2025.

Gevorgian, J., Sandwell, D. T., Yu, Y., et al.: Global distribution and morphology of small seamounts, Earth and Space Science, 10(1), e2022EA002331, 2023.

Gonzalez, R. C. and Woods, R. E.: Digital Image Processing, 4th edn., Pearson, London, 2017.

https://doi.org/10.5194/essd-2026-860
Preprint. Discussion started: 4 November 2026
© Author(s) 2026. CC BY 4.0 License.



Guo, H., Wan, X., and Wang, H.: Validation of just-released SWOT L2 KaRIn beta prevalidated data based on restore the marine gravity field and its application, IEEE Journal of Selected Topics in Applied Earth Observations and Remote Sensing, 17, 7878-7887, 2024.

International Hydrographic Organization: Standardization of Undersea Feature Names: B-6, International Hydrographic Bureau, Monaco, 2008.

Kim, S. S. and Wessel, P.: New global seamount census from altimetry-derived gravity data, Geophysical Journal International, 186(2), 615-631, 2011.

Kitchingman, A. and Lai, S.: Inferences on potential seamount locations from mid-resolution bathymetric data, in: Seamounts: Biodiversity and Fisheries, edited by: Morato, T. and Pauly, D., Fisheries Centre Research Reports, 12(5), Fisheries Centre, University of British Columbia, Vancouver, BC, 7-12, 2004.

Li, Z., Guo, J. Y., Zhu, C. C., Liu, X., Hwang, C., Lebedev, S., Chang, X. T., Soloviev, A., and Sun, H. P.: The SDUST2022GRA global marine gravity anomalies recovered from radar and laser altimeter data: contribution of ICESat-2 laser altimetry, Earth System Science Data, 16, 4119-4135, https://doi.org/10.5194/essd-16-4119-2024, 2024.

Menard, H. W.: Marine Geology of the Pacific, McGraw-Hill, New York, 1964.

Morrow, R., Fu, L.-L., Ardhuin, F., et al.: Global observations of fine-scale ocean surface topography with the Surface Water and Ocean Topography (SWOT) mission, Frontiers in Marine Science, 6, 232, 2019.

Niyazi, Y., Thomas, E. A., Pucino, N., et al.: Status of global seafloor mapping effort and priority areas for future mapping, Frontiers in Marine Science, 12, 1543885, https://doi.org/10.3389/fmars.2025.1543885, 2025.

Otsu, N.: A threshold selection method from gray-level histograms, IEEE Transactions on Systems, Man, and Cybernetics, 9(1), 62-66, 1979.

Ross, T., Du Preez, C., and Ianson, D.: Rapid deep ocean deoxygenation and acidification threaten life on Northeast Pacific seamounts, Global Change Biology, 26(11), 6424-6444, https://doi.org/10.1111/gcb.15307, 2020.

Sandwell, D. T., Goff, J. A., Gevorgian, J., et al.: Improved Bathymetric Prediction Using Geological Information: SYNBATH, Earth and Space Science, 9(2), e2021EA002069, https://doi.org/10.1029/2021EA002069, 2022.

Sandwell, D. T., Harper, H., Tozer, B., et al.: Gravity field recovery from geodetic altimeter missions, Advances in Space Research, 68(2), 1059-1072, 2021.

Sandwell, D. T., Müller, R. D., Smith, W. H. F., et al.: New global marine gravity model from CryoSat-2 and Jason-1 reveals buried tectonic structure, Science, 346(6205), 65-67, 2014.

Sandwell, D. T. and Smith, W. H. F.: Marine gravity anomalies from GEOSAT and ERS-1 satellite altimetry, Journal of Geophysical Research, 102(B5), 10039-10054, 1997.

Staudigel, H., Koppers, A. A. P., Lavelle, J. W., et al.: Defining the word 'seamount', Oceanography, 23(1), 20-21, 2010.

https://doi.org/10.5194/essd-2026-860
Preprint. Discussion started: 4 November 2026
© Author(s) 2026. CC BY 4.0 License.



Tozer, B., Sandwell, D. T., Smith, W. H. F., et al.: Global bathymetry and topography at 15 arc sec: SRTM15+, Earth and Space Science, 6(10), 1847-1864, 2019.

Wang, X., Li, H., Zhang, J., et al.: Seamounts generate efficient active transport loops to nourish the twilight ecosystem, Science Advances, 10(26), eadk6833, https://doi.org/10.1126/sciadv.adk6833, 2024.

Wei, X., Zhang, Y., Shi, X. F., et al.: Geochronological and geochemical constraints on the petrogenesis and geodynamic process of Hemler, Vlinder, and Il'ichev seamount lavas in NW Pacific, Science China Earth Sciences, 67(7), 1856-1871, 2024.

Wessel, P. and Lyons, S.: Distribution of large Pacific seamounts from Geosat/ERS-1: Implications for the history of intraplate volcanism, Journal of Geophysical Research: Solid Earth, 102(B10), 22459-22475, https://doi.org/10.1029/97JB01588, 1997.

Wessel, P.: Global distribution of seamounts inferred from gridded Geosat/ERS-1 altimetry, Journal of Geophysical Research: Solid Earth, 106(B9), 19431-19441, https://doi.org/10.1029/2000JB000083, 2001.

Wessel, P., Sandwell, D. T., and Kim, S. S.: The global seamount census, Oceanography, 23(1), 24-33, 2010.

Wu, Z., Li, J., Yang, F., et al.: An automatic identification and comprehensive judgment method for the foot of continental slope, Acta Geodaetica et Cartographica Sinica, 43(2), 170-177, 2014.

Ya, S., Liu, X., Li, Z., Zhou, R., Bian, S., and Guo, J.: Data interpolation of SWOT/KaRIn blank for modelling marine vertical gradient of gravity anomaly, Geophysical Journal International, 245(1), ggag039, https\://doi.org/10.1093/gji/ggag039, 2026.

Yu, D. and Hwang, C.: Calibrating error variance and scaling global covariance function of geoid gradients for optimal determinations of gravity anomaly and gravity gradient from altimetry, Journal of Geodesy, 96, 61, https://doi.org/10.1007/s00190-022-01647-4, 2022.

Yu, D., Hwang, C., Andersen, O. B., et al.: Gravity recovery from SWOT altimetry using geoid height and geoid gradient, Remote Sensing of Environment, 265, 112650, 2021.

Yu, D., Weng, Z., Hwang, C., et al.: Seamount detection using SWOT-derived vertical gravity gradient: advancements and challenges, Geophysical Journal International, 237(3), 1780-1793, 2024.

Yu, Y., Sandwell, D. T., and Dibarboure, G.: Abyssal marine tectonics from the SWOT mission, Science, 386(6722), 1251-1256, 2024.

Zhou, R. C., Liu, X., Guo, J. Y., et al.: Inverting vertical gravity anomaly gradients using multidirectional data from a mean sea surface model: the case of the Arabian Sea, Earth, Planets and Space, 76, 170, 2024.

Zhou, R. C., Guo, J. Y., Ya, S. S., et al.: SDUST2023VGGA: a global ocean vertical gradient of gravity anomaly model determined from multidirectional data from mean sea surface, Earth System Science Data, 17(2), 817-836, 2025.